RESEARCH ARTICLE

Stability-Centric Design of a Droop-Mounted Adaptive Nonlinear Control for EV Charging in DC Microgrid

AQEEL UR RAHMAN, (Student Member, IEEE), NICOLA CAMPAGNA, (Member, IEEE), FILIPPO PELLITTERI, (Member, IEEE), ANTONINO OSCAR DI TOMMASO, AND ROSARIO MICELI, (Member, IEEE)

Department of Engineering, University of Palermo, 90128 Palermo, Italy

Corresponding author: Nicola Campagna (nicola.campagna@unipa.it)

ABSTRACT This paper presents a streamlined two-layer control system for effective power sharing and switching control in a DC microgrid designed for electric vehicles. The system integrates Energy Storage Systems and advanced converters to ensure a broad operational range and bidirectional power flow. The Dual active bridge topology is used to integrate the EV to DC MG. Hence, the DC MG system has multiple power converter operating simultaneously. The enhanced droop control strategy is advised for the upper layer and the switching controller is derived using nonlinear controls theory embedding the barrier functions. The enhanced droop strategy shares the power considering the individual dynamics of the storage devices while Barrier-based sliding mode control is applied to converters for current/voltage tracking. Mathematical analysis, leveraging Lyapunov's theory, confirms the large signal stability of the system. Demonstrated through MATLAB/Simulink-based simulations, the control system exhibits proficient load power sharing, and the adaptive nonlinear controller showcases robustness against unforeseen disturbances. Moreover, the comparative analysis provides insight into the performance of the proposed control methods concerning traditional methods. Hardware-in-loop tests, utilizing Typhoon HIL 404, authentically validate the real-time performance of the proposed control strategies. Different EV and Constant Power Load scenarios ensure a thorough examination, supporting the efficacy of the system. The study contributes valuable insights into the feasibility and efficiency of these control strategies, paving the way for advancements in sustainable electric mobility.

INDEX TERMS Barrier functions, droop control, electric vehicle charging, large signal stability, microgrids, nonlinear control, power converters.

NOMENCLATURE

Symbol	Quantity
ESS	Energy storage system.
HIL	Hardware-in-the-loop.
CPL	Constant power loads.
MG	Microgrid.
EV	Electric vehicle.
PI	Proportional Integral.
SMC	Sliding mode control.
LQR	Linear quadratic regulator.
FSIBB	Four-switch single inductor buck-boost.

The associate editor coordinating the review of this manuscript and approving it for publication was Min Wang.

BF	Barrier function.
SoC	State of charge.
DAB	Dual active bridge.
V2G	Vehicle-to-grid.
SC	SuperCapacitor.
MPPT	Maximum power point tracking.
MG	Microgrid.
BSMC	Barrier based sliding mode control.
I_{load}	Load Current.
N	Transformer turn ratio.
ϕ	Phase shift angle.
f_{sw}	Switching frequency of the system.
T_{emp}, I_{irr}	Temperature, Irradiance.
τ	Time constant.
R_{droop}	Virtual Resistance.
C_s	Virtual capacitance.
k_i	Controller gains.
a_1, a_2	Positive gain values.
S_i	Sliding Surface.
P_{ev}	Electric vehicle power.
I_L	PV current.
P_{pv}	PV power.
K_i	Integral Gain.
K_p	Proportional Gain.
V_{dc}	DC bus voltage.
e_i	Error values.
V_{in}	Input voltage of PV panels.
V_{Co}	Output voltage of PV system.
I_{bat}	Battery current.
V_{bat}	Battery voltage.
V_{1o}	Output voltage of FSIBB for battery.
D_i	Duty ration of ith FSIBB.
I_{ev}	Charging current for Electric vehicle.
V_{cev}	Electric vehicle voltage level.
V_{2o}	Output voltage of FSIBB for battery.
I_{sc}	SuperCapacitor current.
D	Duty cycle of boost converter.
D_j	Duty cycle of jth FSIBB converters.
T	Switching period of DAB.
$d(t)$	Unbounded time-varying disturbance.

I. INTRODUCTION

DC MGs have gathered significant attention in the energy sector in recent years owing to their notable features: flexibility, efficient controlled power generation, and minimal maintenance costs [1], [2], [3]. With the considerable rise in EV adoption, concerns have emerged regarding the seamless integration of EVs into conventional power networks. DC MG presents a viable alternative solution to address and potentially overcome these integration challenges. Furthermore, DC MGs merge various clean energy sources, including renewable energy sources, and ESS, to offer emission-free solutions [4], [5].

DC MGs present a promising alternative for empowering E-mobility by minimizing issues related to reactive power,

skin effect in transmission lines, and high impedance. These MGs employ power electronics converters to interconnect power sources via a common bus, thereby forming a modern power system based on power electronics [6]. Given the involvement of multiple power converters, stochastic renewable energy sources, and dynamic loads, ensuring the stability and efficiency of DC MGs becomes paramount. Optimal energy management and control strategies [7] are imperative for facilitating uninterrupted EV charging and efficiently handling CPL [8].

In recent years, many multi-layer control algorithms have been proposed for forecasting, power management, and converter control in DC MGs. The CPLs reduce the damping effect of the power converters in DC MGs which can result in instability of the system [9]. Additionally, the inherently nonlinear behavior of power converters [10] necessitates precise control mechanisms to ensure efficient operation. This paper investigates the stability and control perspective of DC MGs for feeding CPLs and charging EVs. Recently, a lot of research has been carried out to improve the efficiency of DC MGs. The droop control method [11] stands as a commonly employed technique for regulating the DC bus voltage and facilitating power-sharing among ESSs. It resolves challenges inherent in centralized control [12] methods by offering a decentralized solution [13]. Reference [14] recommends the utilization of an observer-based droop controller in DC MGs to enhance dynamic response while simultaneously reducing the need for additional current measurements. A proposed approach [15] involves the utilization of an adaptive droop controller followed by a sliding mode controller in a boost converter-based DC microgrid. However, these studies did not consider the problems raised by active loads such as CPLs and EV charging. Some studies [16], [17], specifically discussed the non-linearity of CPLs and tried to solve the problem with optimal control methods. Similarly, heuristic control methods [18], [19] are being explored for energy management in DC MGs. However, concerns arise due to the complexity of design and the high computational costs associated with these methods.

The attention of researchers is directed towards advanced DC-DC power converters [20], due to their high efficiency, wide operating range, and suitability for high-voltage applications [21], [22]. However, they require advanced low-level switching controllers for smooth working. Multiport and high-efficiency bi-directional power converters are developed for EVs and MG applications in [23] and [24], these studies focus on the design and hardware testing of power converters specifically. The system stability and control strategy have not been addressed in these articles. Linear control methods such as PI and LQR are considered state of art control methods for current and voltage regulation [25]. The control design is based on the linearized model of the system operating around its equilibrium point. However, the drawback of this linear control design emerges when the system faces

significant disturbances, potentially impacting its stability. Predictive controllers are proposed to optimally control the power converters in the DC microgrid [26], [27]. Given the nonlinearities inherent in power converters, certain nonlinear control algorithms are recommended for ensuring DC microgrid stability. These algorithms offer rapid dynamic responses and possess the capability to effectively manage unknown disturbances [28], [29], [30]. The review exposed that these studies lack stability analysis concerning the integration of EVs and also exhibit drawbacks, including high computational costs, chattering effects, and reliance on high fixed gains.

This paper focuses on the stability and control of a PV and ESS-based DC microgrid to supply power for EV charging and CPLs. The ESS, comprising batteries and supercapacitors, is employed to face the stochastic behavior of the PV system. It can be employed not only for auxiliary services supply but also to store surplus energy during low-load conditions. The DC bus voltage regulation and power sharing among ESS are facilitated by implementing the decentralized extended droop control algorithm [31]. Additionally, a barrier function-based sliding mode controller [32] is devised for power converters to ensure optimal power extraction. The main contribution of the proposed work can be encapsulated in points as follows:

- A two-layer control framework is proposed to improve the power-sharing, stability, and control effort of the DC microgrid feeding active loads such as EVs and CPLs since the integration and control of the EV charging system is not considered in most DC MG studies;
- Barrier-based SMC adaptive controller is developed for a large-scale system that not only provides the stability analysis but also overcomes the issues associated with traditional nonlinear control methods i.e chattering, high fixed gains;
- Detailed analytical stability analysis is conducted to ensure the global stability of the closed-loop system using Lyapunov theory;
- The proposed algorithm is compared with other linear and nonlinear control methods. Comparative analysis shows the performance of the proposed methods as compared to state of art methods.

The literature review can be encapsulated to show the novelty of the proposed work concerning the combination of different aspects in the table below:

TABLE 1. Comparative analysis of proposed closed-loop system.

Ref.	[31]	[33]	[28]	[34]	**Proposed**
Controller	PI	Deadbeat	SMC	Nonlinear	BSMC
CPL Test	YES	NO	-	NO	YES
EV Integration	NO	NO	NO	YES	YES
HESS Control	YES	YES	-	NO	YES
Large signal Stability	-	NO	YES	YES	YES

The rest of the paper is arranged as follows: Section II deals with the DC microgrid structure and the mathematical modeling of the system. Section III presents a detailed discussion of control derivation and closed-loop stability. Section IV describes the numerical simulation results and discussion to support the proposed strategy. Section V briefly discusses the HIL test and its results. Finally, in section VI the conclusions are given, providing insight into future developments.
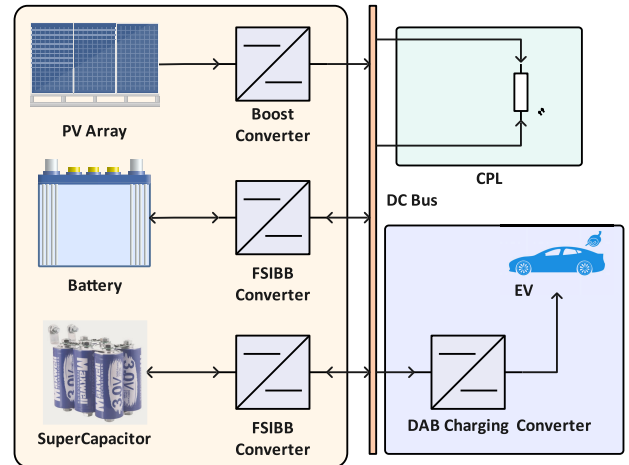

FIGURE 1. Structure of DC microgrid.

II. SYSTEM DESCRIPTION AND MATHEMATICAL MODEL

The block diagram of the DC MG is presented in Fig. 1. The PV modules are connected to the DC bus through a simple boost converter to provide a stepped-up voltage. The FSIBB converter is investigated for integrating a battery and SC-based ESS. Finally, the EV charging integration is managed by the DAB converter. The DC MG also provides the power supply to the CPLs.

A. DC MICROGRID STRUCTURE

The circuit diagram of the power converters deployed in the DC MG is presented in Fig. 2. Mathematical modeling of the system is crucial for understanding the behavior and designing the proper control system. Fig. 2 (a) displays the simple boost converter for PV panels. The PV system is considered the primary power generation source and is intended to operate using MPPT. The average state-space model [35] of the PV-boost module can be represented as:

$$\frac{dI_L}{dt} = \frac{1}{L}(-R \cdot I_L + V_{in} - D \cdot V_{dc}), \tag{1}$$

$$\frac{dV_{Co}}{dt} = \frac{1}{Co}(D \cdot I_L - I_{load}), \tag{2}$$

where I_L, V_{Co}, and I_{Load} represent the inductor current, output voltage, and load current respectively. Similarly, V_{in} and V_{dc} are the input voltage and DC bus voltage, where u denotes the duty cycle of the switch S. The PV current (I_{PV}) can derived through equation shown below:

$$I_{PV} = N_p I_{ph} - N_p I_o \left[e^{\frac{q(V_c + I_c \cdot R_s)}{N_s \cdot A \cdot K \cdot T}} - 1 \right], \tag{3}$$
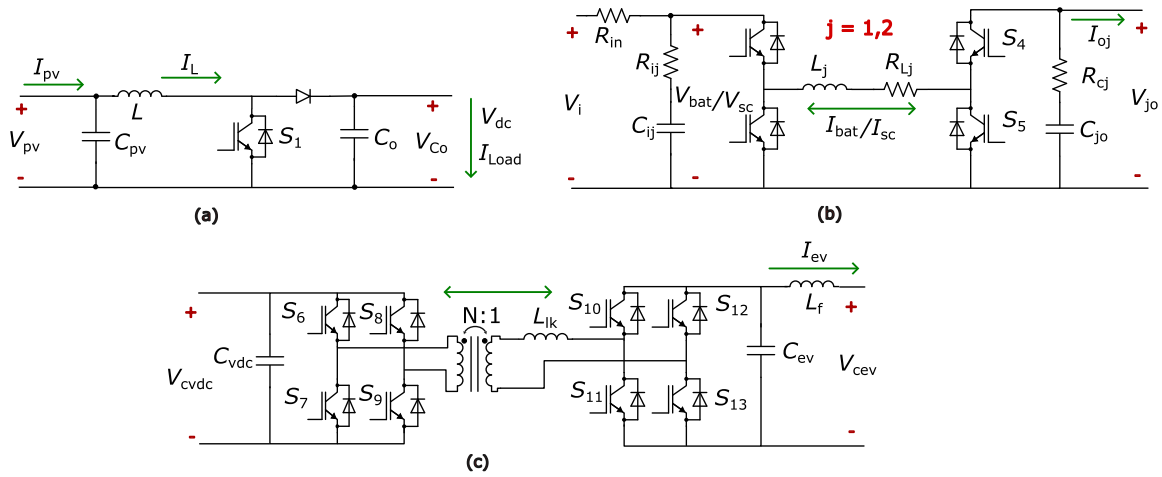
FIGURE 2. Schematic diagrams of the power converters used in DC microgrid (a) Boost converter for PV (b) Four-switches single inductor buck-boost (FSIBB) converter (c) Dual active bridge (DAB converter) for EV.

where N_p represents the number of solar cells connected in a parallel arrangement, I_{ph} signifies the internal photon current, I_o denotes the saturation current, Q stands for the electron charge, V_c indicates the output voltage of the cell, I_c expresses the output current of the cell, N_s defines the number of cells connected in series, A symbolizes the ideality factor, K represents the Boltzmann constant, and T represents the temperature [30].

The ESS, comprising a combination of a battery and SC [36], combines the advantages of both components, offering enhanced storage capacity. Integrating an SC into the ESS aims to manage transient peaks during load changes due to its rapid discharge capability. The investigation into the FSIBB converter topology for the ESS in the DC MG is driven by its advantageous features over traditional buck-boost converters. Fig. 2 (b) shows the circuit diagram of the FSIBB converter deployed with ESS. The large-scale mathematical model of the FSIBB converter is developed by considering two modes of operation: 1) when S_1 and S_3 are conducting and 2) when S_2 and S_4 are ON. The advantages of FSIBB include a non-inverting output, a wide operating range, and an expanded range of operational modes [37]. The design equations for FSIBB can be written as

$$C_{jo} \geq \frac{V_{jo}D_j T_{sw}}{R\delta V_{jo}}, \tag{4}$$

$$L_j \geq V_i \frac{D_j T_{sw}}{\delta I_{L_j}}, \tag{5}$$

where D_j denotes the duty cycle, δV_o and δI_L are the desired ripple values for voltage and current and R represents the output load resistance. The average state-space model can be derived as:

$$\dot{x}_1 = \frac{1}{Lj}(-\frac{R_{ij}R_{cj} + R_{Lj}R_1}{R_1}x_1 + \frac{R_i}{R_1}x_2 + \frac{R_{cj}}{R_1}V_i),$$

$$\dot{x}_2 = \frac{1}{Cj}(-\frac{R_{ij}}{R_1}x_1 - \frac{1}{R_1}x_2 + \frac{1}{R_1}V_i),$$

$$\dot{x}_3 = \frac{1}{C_j}(\frac{-x_3}{R_1}). \tag{6}$$

for the second mode

$$\dot{x}_1 = \frac{1}{Lj}(-\frac{R_{ij}}{R_1}x_1 + \frac{r_i}{R_1}x_3 + \frac{R_1}{V_i}),$$

$$\dot{x}_2 = \frac{1}{Cj}(-\frac{1}{R_1}x_2 + \frac{1}{R_1}V_i),$$

$$\dot{x}_3 = \frac{1}{C_j}(\frac{-x_3}{R_2} + \frac{R}{R_2}x_1), \tag{7}$$

whereas

$$R_1 = R_{in} + R_{ij}, \quad R_2 = R + R_{cj}$$

where $j = 1, 2$ for battery and SC respectively. The averaged model over one switch period can be calculated by finding the average matrices A, B, C, D by using the following expressions

$$\begin{cases} A_{average} = A_{ON}.D_j + A_{OFF}.(1 - D_j) \\ B_{average} = B_{ON}.D_j + B_{OFF}.(1 - D_j) \\ C_{average} = C_{ON}.D_j + C_{OFF}.(1 - D_j) \\ D_{average} = D_{ON}.D_j + D_{OFF}.(1 - D_j) \end{cases} \tag{8}$$

Hence the average state-space model can be obtained as follows:

$$\begin{cases} \dot{x}_k = A_{average} \cdot x + B_{average} \cdot D_j \\ \dot{y}_k = C_{average} \cdot x + D_{average} \cdot D_j, \end{cases} \tag{9}$$

As mentioned before, the FSIBB converter has two modes of operation buck and boost, the equation (8) calculates the average state-space matrices over a complete duty cycle. Equation 9 represents the general state-space form of the model [38]. Where $k = 1, 2 \ldots.6$ for both battery and supercapacitor, respectively. $A_{average}, B_{average}, C_{average}, D_{average}$ are the calculated average value matrix, obtained by combining equations (6,7). For more clarity, it can be expressed as

$$[x_1, x_2, x_3, x_4, x_5, x_6]^T = [I_{bat}, V_{bat}, V_{1o}, I_{sc}, V_{sc}, V_{2o}]^T.$$

The system parameters are given in table 2.

TABLE 2. DC microgrid parameters and values.

PV system	
Parameter	**Values**
Number of panels (series * Parallel)	10*10
Capacitance C_{pv}, C_o	7 , 400 μF
Inductor L_{pv}	7.22 μH
Power at MPPT P_{pv}	21.315 kW
Energy Storage System (ESS)	
Battery nominal Voltage	100 V
Rate Capacity	100 Ah
Battery response time	0.1 s
Initial SoC battery	75 $\%$
SuperCapacitor rate voltage	48 V
Number of capacitors in SC	6*8
Rate capacitance of SC	100 F
FSIBB Converter	
Input Resistance R_j	220 $\mu \Omega$
C_{ij} Input Capacitance	680 μF
Inductance value L_j	220 μH
Internal Resistance R_{Lj}	1.4 mΩ
Output capacitance	200 μF

B. EV CHARGING STRUCTURE

The EV integration with the DC MG is reached through the DAB converter. Illustrated in Fig. 2 (c), the circuit diagram of the DAB converter features two full bridges and an isolating transformer, complemented by an inductor. Isolated DC-DC converters are gaining prominence due to their compliance with high-power applications. Their bi-directional power flow capability plays a pivotal role in Grid-to-Vehicle (G2V) and V2G operations, facilitating efficient DC fast charging of EVs [39]. The DAB converter encompasses components such as C_{vdc}, the input side capacitor, L_{lk}, the inductor, and an output filter comprising C_{ev} and L_f. The expression for the output power of the DAB converter can be depicted as:

$$P_{ev} = \frac{N V_{Cev} V_{Cvdc} \phi (1 - 2|\phi|)}{f_{sw} L_{lk}}.$$ (10)

Here, P_{ev} signifies the output power of the DAB converter, while N, ϕ, and f_{sw} represent the transformer number of turns, phase shift, and switching frequency, respectively. In the case of an ideal transformer, the number of turns can be expressed as:

$$N = \frac{V_{cev}}{V_{cvdc}}.$$ (11)

The mathematical model of the DAB converter can be derived by using the state-space average technique [34] and can be written as:

$$\dot{x}_7 = -\frac{R}{L_{lk}} x_7 + \frac{T \cdot R \cdot N}{L_{lk}^2} \cdot \phi (1 - 2|\phi|) x_9,$$

$$\dot{x}_8 = \frac{1}{C_{ev}} x_7 + \frac{1}{R_{ev} C_{ev}} x_8 + \frac{V_g}{R_{ev} C_{ev}},$$

$$\dot{x}_9 = \frac{N}{C_{vdc}} x_7 - \frac{1}{R_g C} x_9 + \frac{V_{ev}}{R_g C_{vdc}}.$$ (12)

ϕ serves as the control parameter employed for regulating the output power of the DAB through phase shift modulation. Where R_g and R_{ev} denote the MG side resistance and EV side

resistance, respectively. The state variables of the system are defined as:

$$[x_7, x_8, x_9]^T = [I_{ev}, V_{cev}, V_{cvdc}]^T.$$

The current and voltage characteristics of CPL are illustrated in a mathematical expression given below

$$I_{load} = \frac{P_{CPL}}{V_{CPL}}.$$ (13)

The large signal model of the DC MG is represented by equations (1), (2), (8), and (12). This mathematical model serves as the foundation for analytically deriving control methodologies for the system. A comprehensive design analysis is conducted in the subsequent section.

TABLE 3. DAB-based charging interface.

EV Battery	
Parameter	**Values**
EV battery nominal voltage	400 V
EV battery capacity	80 kWh
Initial SoC of EV battery	60 $\%$
EV battery response time	1 s
Battery type	Lithium-ion
DAB Converter	
Parameter	**Values**
Grid side capacitance C_{vdc}	$60e^{-6}$ F
Turns ratio of transformer	1 : 1
Inductor value L_{kl}	$1.3e^{-05}$ H
EV side capacitance C_{ev}	3.00 mF
Filtering Inductance L_f	$3.36e^{-05}$ H

III. ADAPTIVE CONTROL STRATEGY

In this section, the adaptive control strategy is fully described. In particular, the first subsection focuses on droop-based supervisory control, responsible for power-sharing between the ESS and DC bus voltage regulation; the second subsection discusses the detailed derivation of the barrier-based non-linear controller for power converters. Finally, the third subsection studies the closed-loop stability analysis using Lyapunov theory. The closed-loop PV system is designed to operate at MPPT. To achieve this condition, an MPPT controller is recommended to extract the maximum power, which is contingent upon temperature and irradiance values. As weather parameters influence PV power, the output PV power remains variable rather than constant. The optimized linear regression [40] gives the expression to get the MPP using the temperature and irradiance value and expressed as

$$V_{mppt} = 332 + 1.34 \cdot T_{emp} - 0.00964 \cdot I_{irr}.$$ (14)

Here, V_{mppt}, T_{emp}, and I_{irr} represent the MPPT voltage, temperature value, and irradiance, respectively. The expression determines the maximum power point, while a PI controller tracks the reference value and attains maximum output power.

A. PRIMARY-LEVEL DROOP CONTROL

The paper introduces a two-layer control strategy focusing on power-sharing and converter switching to maintain system

stability. The upper control layer is specifically developed to facilitate power distribution between the storage system and regulate the DC bus voltage. The primary objective of the ESS is to offer auxiliary support during power shortages. This objective can be effectively met with a well-designed energy management system. An enhanced droop control method is proposed due to its simplicity and good performance. The current request from ESS can be expressed as

$$I_{ESS} = I_{load} - I_{PV}. \tag{15}$$

The I_{ESS} can be shared between the battery and SC in such a way that high peak dynamics are managed by SC and base power is handled by the battery. The expressions can be written as

$$
\begin{aligned}
I_{o1} &= G_1(s) \cdot I_{ESS}, \\
I_{o2} &= G_2(s) \cdot I_{ESS},
\end{aligned} \tag{16}
$$

where

$$
\begin{aligned}
G_1(s) &= \frac{1}{1 + \tau \cdot s}, \\
G_2(s) &= \frac{\tau \cdot s}{1 + \tau \cdot s}.
\end{aligned} \tag{17}
$$

τ is the time constant which can be expressed as $\tau = \frac{1}{RC}$ · $G_1(s)$ and $G_2(s)$ represent the low and high pass filters respectively. The time constant τ should be greater than or equal to the battery response time so that the battery can respond according to droop control signals [31]. The V/I relationship of battery and SC can be expressed as:

$$V_{o1ref} = V_{vdcref} - R_{droop} \cdot I_{o1}, \tag{18}$$

where R_{droop} is the virtual resistance incorporated to regulate the DC bus voltage through the storage system. The R_{droop} can be expressed mathematically as [31]:

$$R_{droop} = \frac{V_{dcmax} - V_{vdcmin}}{I_{omax}}. \tag{19}$$

V_{vdcmin} and V_{vdcmax} are the maximum and minimum allowable DC bus voltage. I_{omax} is the maximum allowable current of the FSIBB converter. Contrary to the virtual resistance concept, the SC voltage reference is derived using a virtual capacitance method. The value of virtual capacitance for the particular case can be found by solving the time constant τ and R_{droop}. The expression of SC voltage reference can be formulated as:

$$V_{o2ref} = V_{dcref} - \frac{1}{C_s} \cdot I_{o2}. \tag{20}$$

Here, C_s represents the virtual capacitance, contributing to a quicker dynamic response than virtual resistance. The fundamental concept involves enhancing the traditional droop controller by integrating virtual capacitance, enabling it to effectively manage abrupt load variations while supporting DC bus voltage regulation. PI regulators are configured to generate the current reference for the battery and SC. The inner control loop is subsequently responsible for tracking the current reference and ensuring system stability.

B. BARRIER-BASED ADAPTIVE NONLINEAR SWITCHING CONTROLLER

The significance of the low-level switching controller is pivotal for ensuring system stability. Its primary function involves controlling the converter and toggling it on and off to achieve the desired power output. Given the nonlinear characteristics inherent in power sources and converters, the proper design of this control algorithm is crucial. To address this challenge, this study introduces a proposed barrier function-based adaptive nonlinear controller. This controller not only ensures system stability but also mitigates the overestimation of gains while resisting external disturbances. Fig.3 shows the flowchart representation of the adaptive control algorithm. In this subsection, the derivation of the
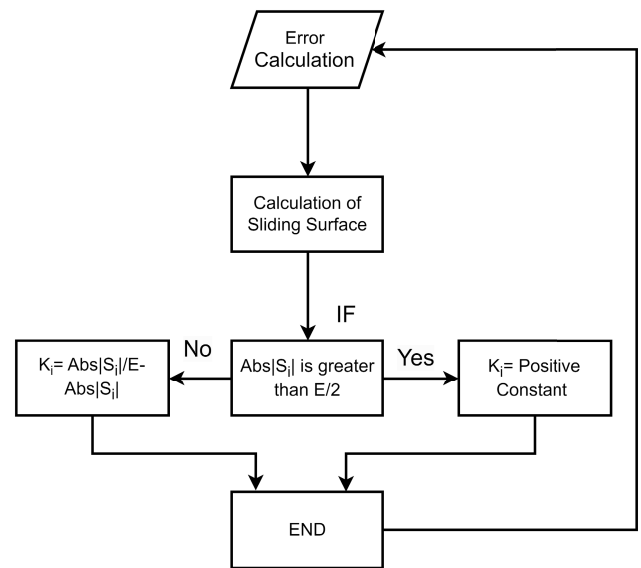

FIGURE 3. Flowchart representation of barrier-based adaptive gains.

low-level controller is explained step by step. In the tracking controller, the error signals are the starting points, the error is defined as the difference between the actual and desired value of the state and it can be written as

$$
\begin{aligned}
e_1 &= x_{1ref} - x_1, \\
e_2 &= x_{4ref} - x_4,
\end{aligned} \tag{21}
$$

where the reference for the battery and SC current can be obtained by solving the equation (18) and (20) as:

$$x_{1ref} = K_p(V_{o1ref} - x_3) + K_i \int_0^t (V_{o1ref} - x_3)dt,$$

$$x_{4ref} = K_p(V_{o2ref} - x_6) + K_i \int_0^t (V_{o2ref} - x_6)dt. \tag{22}$$

Different sliding surfaces are selected to keep the controller fully decentralized, the sliding surfaces are shown below:
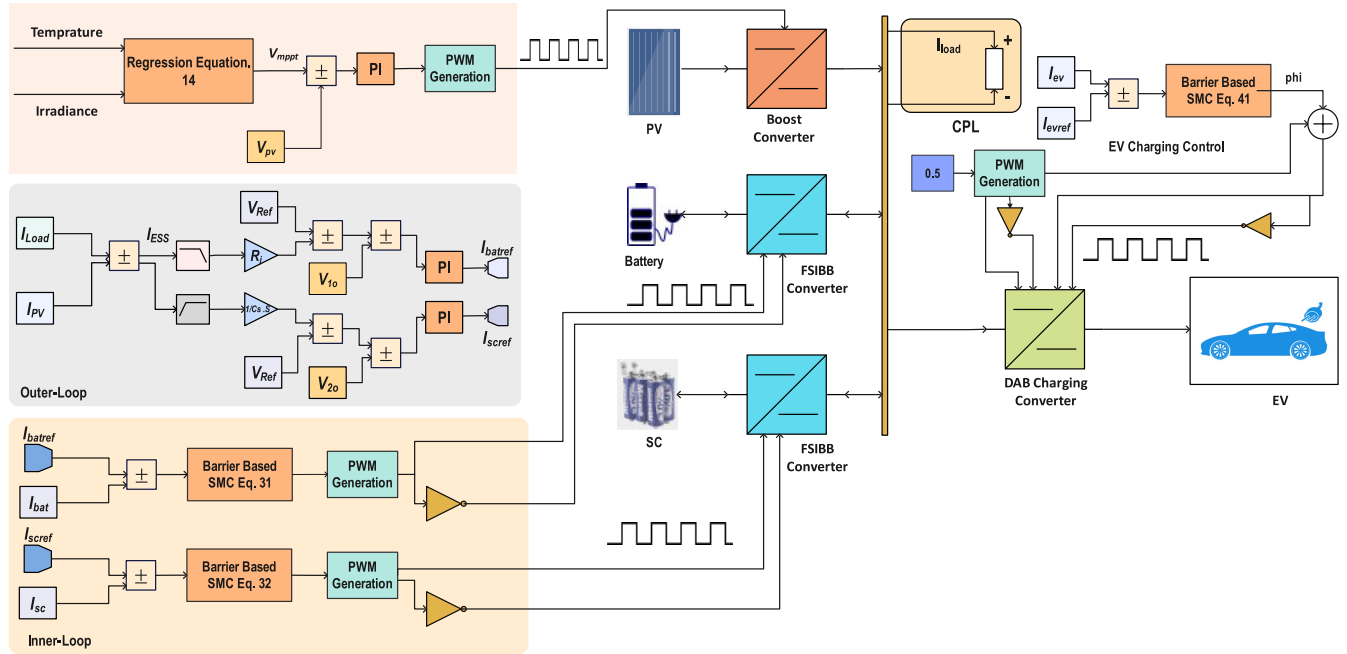
$$S_1 = a_1 e_1, \tag{23}$$

$$S_2 = a_2 e_2. \tag{24}$$

FIGURE 4. Proposed dual-loop control mechanism for DC microgrid.

Taking the time derivative of the equations above results

$$\dot{S}_1 = a_1 \dot{e}_1, \tag{25}$$

$$\dot{S}_2 = a_2 \dot{e}_2, \tag{26}$$

Here, a_1 and a_2 are the positive gains used to give the specific weight to the error signal, and $\dot{e}_1$, $\dot{e}_2$ gives the response of the error signals with time. It is possible to assume

$$\dot{S}_i = -k_i \, |S_i|^{0.5} \, sgn\left(\frac{S_i}{0.5}\right), \tag{27}$$

where $i = 1, 2, 3$, k_i denotes the controller gain which can be fixed or adaptive depending on the BF. The idea is to fix a gain initially which can bring the sliding surface $S_i(t)$ near the zero $\epsilon/2$, the gain switches to the BF to keep the trajectory in the neighborhood of zero. The definition of the barrier function can be illustrated by theorems given in [32].

Definition of BF: It can be supposed that the ϵ is fixed and has a value near zero, then the BF can be defined as a continuous function $k_i(y) : y \in]-\epsilon, \epsilon[\rightarrow k_i(y) \in]b, \infty[$ increasing on $[0, \epsilon]$.

- $\lim_{|y| \to \epsilon} k_i(y) = +\infty$
- $k_i(y)$ has a unique minimum at zero and $k_i(0) = i \geq 0$

The considered BF in this case is defined as

- The positive semi-definite BF is selected to derive the control law as: $K_i(y) = \frac{|y|}{\epsilon - |y|}$

Hence, the adaptive gains for S_i can be expressed mathematically as:

$$k_i(t, S_i(t)) = \begin{cases} k_a(t), \dot{k}_a(t) = \bar{k}|S(t)| & if \quad 0 \leq t \leq \bar{t}, \\ k(S(t)) & if \quad t \geq \bar{t}, \end{cases} \tag{28}$$

$$k_i(S(t)) = \frac{|S_i|}{\varepsilon - |S_i|}. \tag{29}$$

The equations (25) and (26) can be expanded as:

$$\dot{S}_1 = a_1(\dot{x}_{1ref} - \dot{x}_1), \tag{30}$$

$$\dot{S}_2 = a_2(\dot{x}_{4ref} - \dot{x}_4). \tag{31}$$

The value of $\dot{x}_1$ and $\dot{x}_4$ can be taken from equation (8), solving it for control variable $u_j, j = 1, 2$ gives:

$$D_1 = \frac{9.86e^3 x_1 a_1 + 4.46e^4 x_3 a_1 + a_1 x_1\dot{r}_{ef} - k_1 \, |S_1|^{0.5} \, sgn\left(\frac{S_1}{0.5}\right)}{6.69e^3 x_1 a_1 + 1.42e^4 x_2 a_1 + 31250 V_i a_1 + 4.04 x_3 a_1}, \tag{32}$$

$$D_2 = \frac{9.86e^3 x_4 a_1 + 4.46e^4 x_6 a_1 + a_1 x_1\dot{r}_{ef} - k_2 \, |S_i|^{0.5} \, sgn\left(\frac{S_1}{0.5}\right)}{6.69e^3 x_4 a_1 + 1.42e^4 x_5 a_1 + 31250 V_{isc} a_1 + 4.04 x_6 a_1}. \tag{33}$$

Hence, D_1 and D_2 are the control inputs applied to the FSIBB converters in ESS. The control inputs are the same in the diagonal of the H-bridge and inverse in the same leg switches. Similarly, the charging controller for EV charging is designed using the same method. However, for the EV charging controller, the direct current control method is adopted. The EV can be charged with a power level equal to $12kW$ or with a lower one to reduce the stress on the DC MG with normal charging. The DAB converter is used for interaction between the EV battery and DC MG, the error

function for DAB current can be expressed as:

$$e_3 = x_{7ref} - x_7. \tag{34}$$

Taking the time derivative of the error error signal returns

$$\dot{e}_3 = \dot{x}_{7ref} - \dot{x}_7. \tag{35}$$

Putting the value of $\dot{x}_7$ from DAB model given in equation (12), $\dot{e}_3$ can be expressed as:

$$\dot{e}_3 = \dot{x}_{7ref} + \frac{R}{L_{lk}}x_7 - \frac{T \cdot R \cdot N}{L_{lk}^2} \cdot \phi(1 - 2|\phi|)x_9. \tag{36}$$

The sliding surface for control law derivation is assumed as:

$$S_3 = a_3 e_3 \Rightarrow \dot{S}_3 = a_3 \dot{e}_3. \tag{37}$$

The sliding surface contains the error signal with a positive gain a_3. It means that the error trajectory would not converge easily to a chosen surface. Using the assumption given in equation (27) and putting the value of $\dot{e}_3$, it can be stated:

$$-k_3 |S_3|^{0.5} sgn\left(\frac{S_3}{0.5}\right) = \dot{x}_{7ref} + \frac{R}{L_{lk}}x_7 - \frac{T \cdot R \cdot N}{L_{lk}^2}.\phi(1 - 2|\phi|)x_9. \tag{38}$$

Solving it for control variable ϕ gives

$$\phi(1 - 2|\phi|) = \frac{L_{lk}^2}{T \cdot R \cdot N \cdot x_9}\left(\dot{x}_{7ref} + \frac{R}{L_{lk}}x_7 + k_3 |S_3|^{0.5} sgn\left(\frac{S_3}{0.5}\right)\right). \tag{39}$$

To simplify the solution, it can be rearranged as

$$\phi(1 - 2|\phi|) - T = 0 \Rightarrow \phi - 2\phi^2 - T = 0, \tag{40}$$

where T can be written as:

$$T = \frac{L_{lk}^2}{TRNx_9}\left(\dot{x}_{7ref} + \frac{R}{L_{lk}}x_7 + k_3 |S_3|^{0.5} sgn\left(\frac{S_3}{0.5}\right)\right). \tag{41}$$

Finally, the control law is obtained by solving the polynomial of equation (40) as:

$$\phi = \frac{-1 - \sqrt{1 - 8T}}{-2}, \quad \phi = \frac{-1 + \sqrt{1 - 8T}}{-2}. \tag{42}$$

The control variable ϕ is represented per unit value within the $-0.5 \leq \phi \leq 0.5$. This phase-shift angle is critical in modulating the power level within the DAB power converter. Consequently, in this scenario, it constitutes the ultimate control law employed for direct current regulation in the DAB converter. Fig.4 shows the overall block diagram of the proposed method. The outer loop is based on the droop strategy and distributes the power among ESS. The inner loop is designed to generate the switching signals for power converters. The MPPT control algorithm for the PV system is also shown in the figure.

C. CLOSED-LOOP STABILITY ANALYSIS

Closed-loop system stability is essential for designing a large system controller. Lyapunov theory be used to provide insight stability analysis for the model-based controllers where large signal models are considered. The Lyapunov candidate function can be selected to start the stability analysis. The criteria for selecting a Lyapunov candidate can be summed in the following points:

- The lyapunove candidate function V should be positive definite $V(S_i) \geq$ for all values of S_i,
- If $S_i \to 0$ then $V(S_i) \to 0$.

Based on theoretical rules, the Lyapunov function can be expressed mathematically as:

$$V = \frac{1}{2}S_1^2 + \frac{1}{2}S_2^2 + \frac{1}{2}S_3^2. \tag{43}$$

The Lyapunov candidate function accommodates all the sliding surfaces that contain the error signals so that the stability of the DC MG can be determined. Lyapunov function is an energy function depicting the energy of the physical system. Taking the time derivative of the Lyapunov candidate function, it gives

$$\dot{V} = S_1\dot{S}_1 + S_2\dot{S}_2 + S_3\dot{S}_3, \tag{44}$$

which can be simplified as:

$$\dot{V}(S_i) = S_i\dot{S}_i. \tag{45}$$

Putting the error e_1, e_2, e_3 and control input values from equations (32,33,42), the expression above take the form:

$$\dot{V}(S_i) = S_i(-k_i |S_i|^{0.5} sgn\left(\frac{S_i}{0.5}\right)), \tag{46}$$

where

$$|S_i|^{0.5} \geq 0, \quad S_i(-k_i sgn\left(\frac{S_i}{0.5}\right)) \geq 0. \tag{47}$$

Remark 1: The function $S \cdot sgn(S)$ consistently yields a positive value due to the nature of the signum function, resulting in $+1$ for positive function values and -1 for negative ones. This signum function is the switching control, maintaining the system on the desired trajectory. However, it is prone to chattering issues, which can be mitigated through appropriate gain adjustments.

Finally, we get

$$\dot{V}(S_i) \leq 0, \ for \ all \ S_i \in \mathbb{R}. \tag{48}$$

As stated by the expression above, the time derivative of the Lyapunov function is negative definite which means that the closed-loop system is globally stable and all the error values should converge to the equilibrium point when time $t \to 0$.

IV. SIMULATION RESULTS AND DISCUSSION

The section discusses simulation studies and the outcomes of the proposed method. Numerical simulations are conducted to validate the proposed algorithms. Additionally, the closed-loop system is tested under various conditions to evaluate the controller response. Subsequent subsections provide detailed discussions of the results.
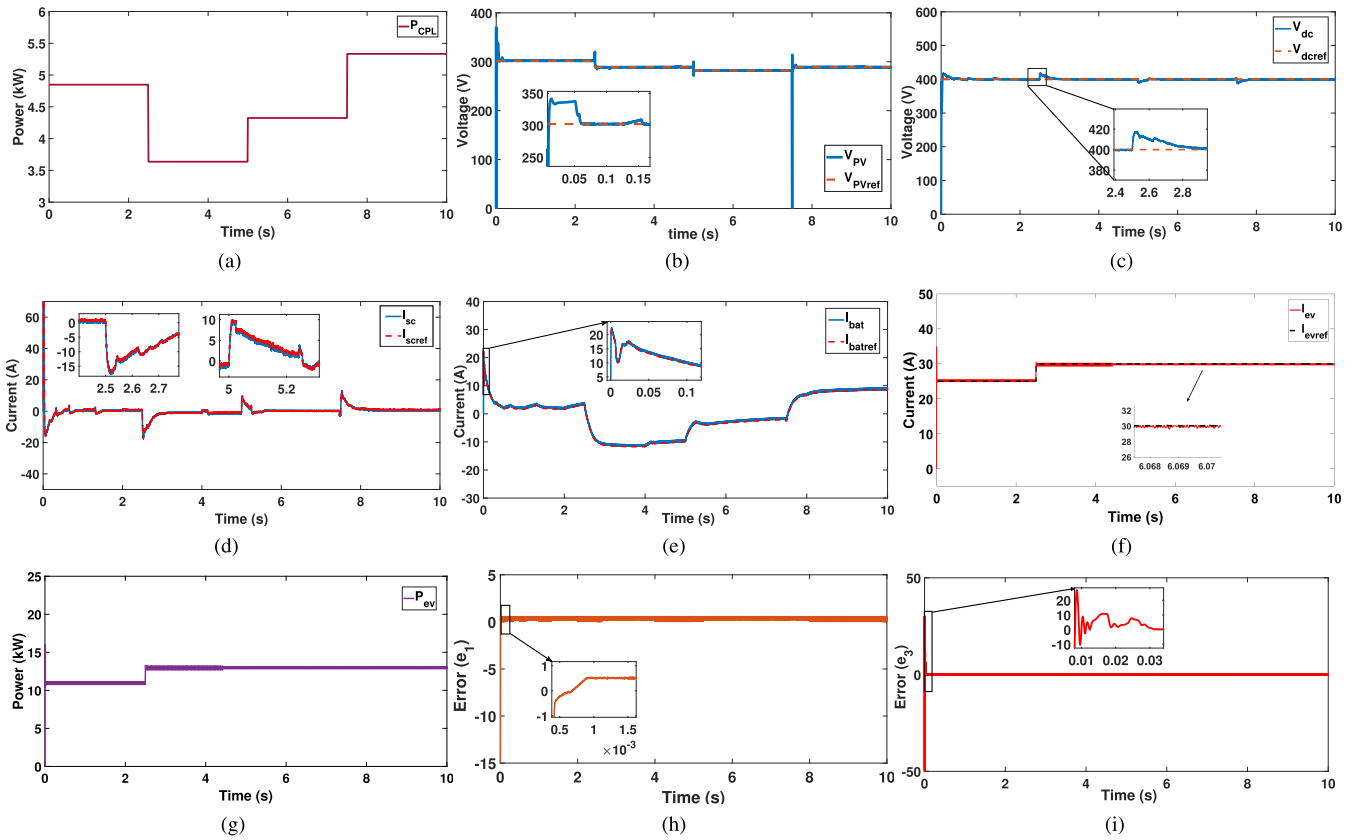
FIGURE 5. (a) Time-varying load power of CPL (b) PV voltage V_{pv} at MPPT (c) DC bus voltage (V_{dc}) response (d) SuperCapacitor Current (I_{sc}) response (e) Battery current (I_{bat}) in DC microgrid (f) Charging Current for EV in DC microgrid (g) EV charging power in DC microgrid (h) Plot of error (e_1) (i) Graph of EV current error (e_3).

A. NUMERICAL SIMULATIONS

The DC MG system is simulated in MATLAB/Simulink (R2023 b) environment using the simscape library. The simulation results are shown in Fig. 5 with 9 sub-figures (a)-(l). A time-varying CPL is considered which can be seen in Fig. 5a and mathematically expressed as:

$$P_{CPL} = \begin{cases} 4.7 \, kW, & if \quad 0s \le t < 2.5 \, s \\ 3.3 \, kW, & if \quad 2.5 \, s \le t < 5 \, s \\ 4.3 \, kW, & if \quad 5 \, s \le t < 7.5 \, s \\ 5.35 \, kW, & if \quad 7.5s \le t \le 10 \, s \end{cases} \quad (49)$$

Fig. 5b displays the PV voltage response with the MPPT controller. The figure illustrates two trajectories, where the red dotted line represents the desired Maximum PowerPoint (MPP), and the blue line represents the response of V_{PV}. The temperature and irradiance values vary within the range of $20 - 35$ Celsius degrees and $700 - 1000 W/m^2$, respectively. It is evident from the figure that the PV voltage can properly track its reference. Similarly, Fig. 5c represents the DC bus voltage response, one of the main aims of upper layer control is to regulate the DC link voltage to the desired value equal to $V_{dcref} = 400$. Since one graph shows both the reference line and the actual state value it can be verified that the DC bus voltage is regulated with little spikes at $t = 0, 2.5, 5, 7.5s$.

These overshoot/undershoots are due to time-varying load as mentioned in the equation (49). However, with the proposed control, the fluctuations are within the limits $\pm 4\%$.

The second interesting aspect to analyze is the response of the ESS. The control scheme is devised so that the battery supplies the base current, yet it exhibits a slow response. This sluggish response is effectively compensated by the fast dynamic reaction of the SC. Graphs for the battery and SC are presented in Figs. 5d and 5e, respectively. The SC provides a rapid dynamic response during load changes, complementing the slower response of the battery. Additionally, the graphs illustrate the tracking of battery and SC current in a zoomed-in area, showcasing the efficacy of the low-level adaptive nonlinear controller. Figs. 5d and 5e depict the tracking of desired reference values (indicated by a red dotted line), confirming the stability of the system.

The scope of the study also involves the integration and charging of EVs which can be controlled by deploying a direct current-controlled DAB converter. The charging current waveform is plotted in Fig. 5f, to verify the charging control, the EV is charged with two different current values (25A, 30A). It can be seen that the EV charging current is tracking the different current levels which validates the charging control performance. The zoomed-in figure shows the steady-state performance of the advised control, the graph
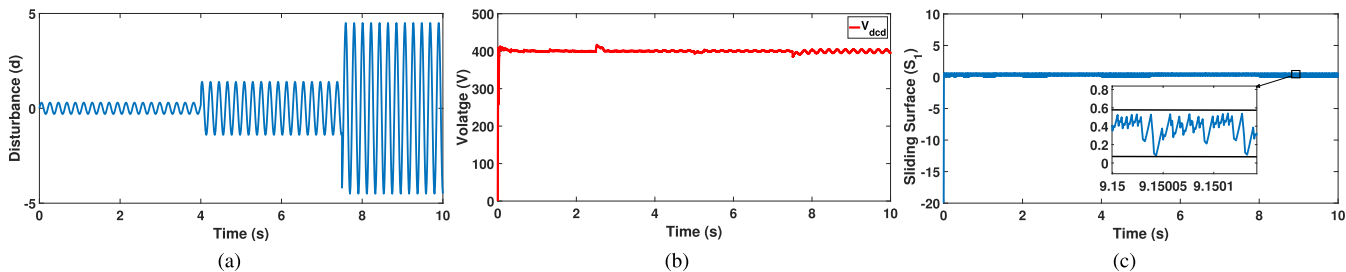
FIGURE 6. Robustness Test (a) Unknow time-varying disturbance d (b) Response of DC bus voltage against disturbance (c) Sliding surface S_1 response.

shows that the controller has a steady-state error of 0.5A. Similarly, Fig. 5g shows the charging power of the EV charger. The charging power level also changes with the change in charging current. The maximum charging power is 13.5 kW for the 400V EV battery.

TABLE 4. Parameters of proposed Controllers for testing.

Enhanced Droop Control	
Parameter	Values
Time constant τ	0.5 s
Virtual Resistance R_{droop}	0.033 Ω
PI regulator for battery K_p	0.05
PI regulator for battery K_i	5
PI regulator for SC K_p	1
PI regulator for SC K_i	0.5
Adaptive Nonlinear Control	
Parameter	Values
a_1, a_2, a_3	1.00
ϵ	0.5
k_1, k_2, k_3	$5e^6$, $5e^6$, 7000
Sliding surface S_i	0

The initial SoC of the EV battery is intentionally set to a low value of 60%. It is noticeable that when the charging power level varies within the range of (25A − 30A), the SoC trajectory also alters its behavior, indicating a rapid charging behavior. The Lyapunov stability analysis ensures the convergence of error signals to zero, Figs. 5h and 5i depict the error signal reaction to the applied control strategy, and the magnified portion shows the transient response of the error trajectory however when the control acts the error signals converge to zero. It can be concluded from the error signal that the adaptive nonlinear controller can remove the steady-state error and keep the system stable in different scenarios. The control parameters used to develop the control algorithm are listed in the table 4. The PI gains for the outer loop droop control are adjusted by using the error and trial method to avoid the complexity of the design. However, many methods can be found in the literature to tune the PI controller.

B. ROBUSTNESS TEST

The robustness test is conducted to evaluate the performance of the proposed controller in the presence of external disturbance. A time-varying disturbance is incorporated with an unknown upper bound in this case. One of the advantages of barrier function-based nonlinear controllers is that they

can mitigate the effect of disturbances and keep the system stable. The mathematical expression for the time-varying
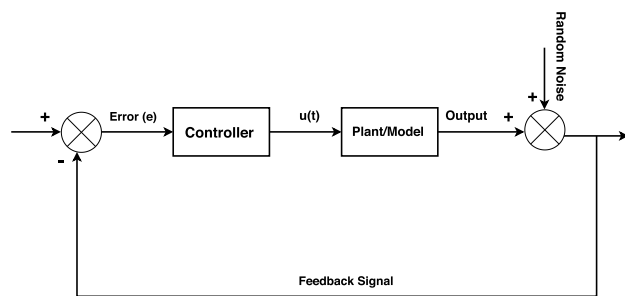

FIGURE 7. Closed-loop system with disturabnce.

disturbance can be written as:

$$d(t) = \begin{cases} 0.3sin(t), & if \quad 0 \le t < 4.5s \\ 1.4sin(t), & if \quad 4.5s \le t < 7.5s \\ 4.8sin(t), & if \quad t \ge 7.5s, \end{cases} \quad (50)$$

Fig. 6a, shows the graph of disturbance d, a sinusoidal function with varying amplitude. The response of DC bus voltage V_{dc} is plotted against disturbance d in fig.6b. The result proves system stability as DC bus voltage is regulated to 400. However, little effect of the disturbance can be observed after $t = 7.5$ which is in the limit of ± 4 due to the tight adaptive controller. The result shows the system stability and voltage regulation in the presence of unknown disturbance with unknown upper and lower bounds. The adaptive gains and barrier-based control structure can minimize the effect of unknown disturbance significantly. Finally, Fig. 6c presents the response of sliding surface S_1 in the presence of disturbance. The magnified section of the figure depicts the effect of disturbance on the sliding surface however the important aspect to notice is the amplitude of the disturbance at $t \ge 7.5s$ is 4.8 but the S_1 has a variation of value 0.3. In light of these results, it can be stated that the adaptive nonlinear controller showed robustness against unknown disturbance and minimized the effect by keeping the trajectory on the desired sliding surface. Fig. 7 shows the block diagram of the system with the disturbance. In this paper, the idea of barrier function-based adaptive control is used to manage unknown disturbances, and the disturbance

signal is added to the DC bus. The idea is to test the system's robustness against an unknown disturbance signal with an unknown upper bound. So, a sinusoidal function has been considered with varying upper bounds.

C. COMPARATIVE ANALYSIS

The proposed controller is compared to state-of-the-art control algorithms such as PI, the Lyapunov method, and traditional SMC. DC bus regulation is selected as a criterion to compare different algorithms and the comparative graph is presented in fig. 8. The three zoomed-in sections (1,2,3) depict the transient response, overshoot/undershoot, and steady-state behavior of the control methods. It can be seen that the proposed control method shows the optimal response while maintaining the minimum tracking error. The proposed controller has less error, overshoot/undershoot, and peak value as compared to others. Traditional SMC has a fast response but also has the problem of chattering and high over/undershoots. The problem is catered by power rate reaching law and adaptive gains in the proposed method. Table 5 presents the comparative data of different controllers for a better understanding.
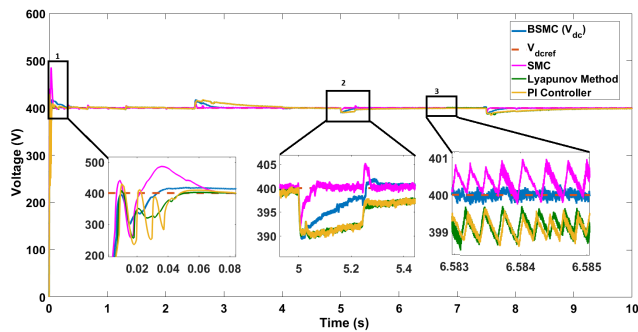

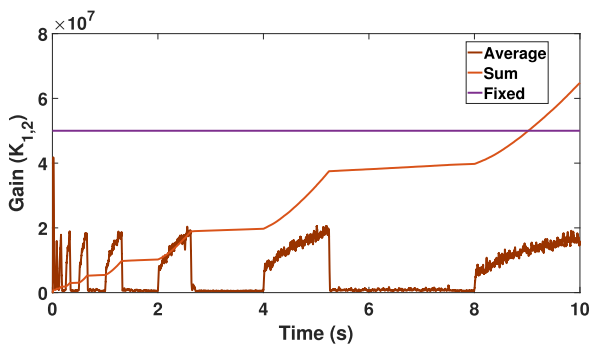**FIGURE 8.** Comparative graph of different control methods.

FIGURE 9. Comparative Analysis of different gains.

The fixed and variable gains k_i of the adaptive nonlinear controller are plotted in the same graph and presented in Fig. 9. The embedding barrier function can be understood by analyzing the gains graph. The three different colored trajectories (brown, orange, and purple) are plotted in a

single figure, the comparative analysis demonstrates that the controller gains are reduced up to notable values and the targeted results are achieved with comparatively fewer control efforts as of fixed gains. Moreover, the sum of adaptive gains is also displayed in Fig.9.

TABLE 5. Comparative analysis of proposed controller.

Sr.	Rise time	Over/undershoot	Error	Peak value
PI	6.525 ms	8.152% ,41.26%	1.1	429.8
Lyapunov	6.2 ms	7.2% ,39.26%	0.9	425.8
SMC	4.192 ms	9.787% , 36.617%	0.67	485.2
Proposed	5.237 ms	2.673%, 35.503%	0.095	417.2

V. REAL-TIME HARDWARE-IN-LOOP TEST

The high-fidelity HIL test is then conducted to affirm the real-time performance of the proposed controller. The Typhoon HIL 404 emulator is employed to instantiate the DC microgrid, utilizing the FPGA cores of the device. The closed-loop controller operates in real-time, utilizing system cores. The Typhoon HIL also furnishes the HIL SCADA, enabling real-time control over the operational system. The outcomes can be visualized through an oscilloscope connected to the Typhoon HIL. For real-time analysis, varying CPLs are employed, with the initial SoC of the storage system set to 75%. The assumed operating conditions include the PV system functioning under MPPT at a temperature of 25 C and irradiance of 1000 W/m^2.
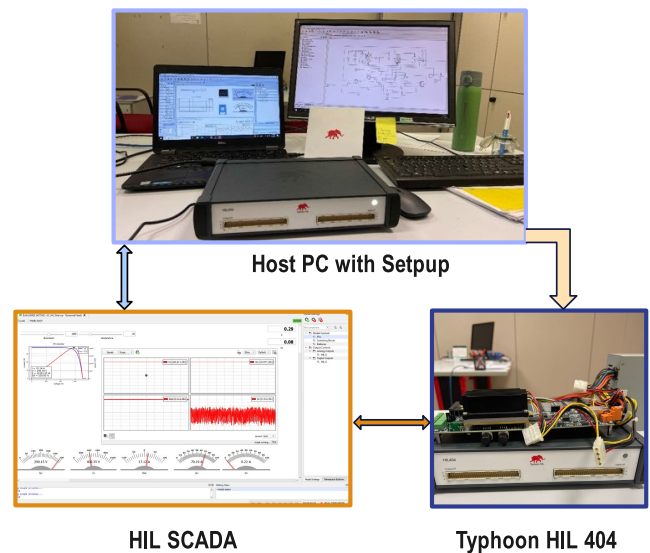

FIGURE 10. Hardware-in-Loop Setup for real-time testing.

The HIL results are shown in Fig. 11, Fig.11a shows the varying load profile while Fig. 11b illustrates the MPPT working of the PV system at specific weather parameters. To verify the control objective, the DC bus voltage response is plotted in Fig. 11c, the reference value for the DC bus voltage is considered 400V, the same as in simulation tests. The response of ESS is also reported in Fig. 11d and 11c,
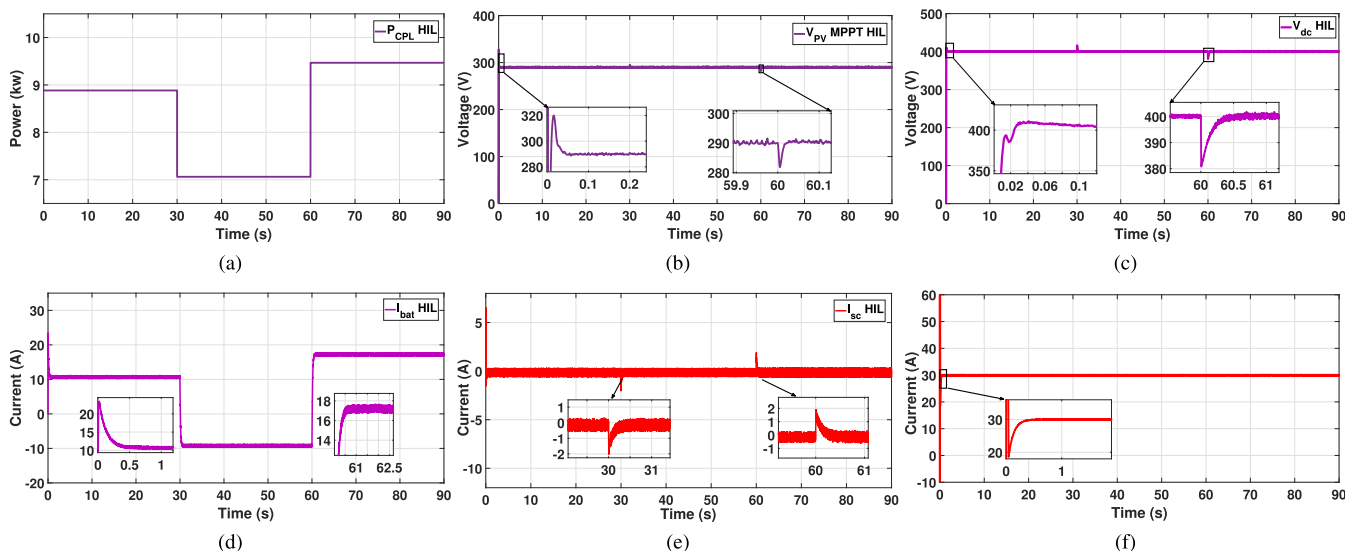
FIGURE 11. Hardware-in-loop based real-time results (a) Time-varying load power (b) PV voltage at MPPT in real-time (c) DC bus voltage response (d) Battery current response with charging and discharging (e) Super Capacitor current response (f) EV charging current in real-time.

respectively. Lastly, Fig. 11e indicates the behavior of the charging current of the integrated EV. The reference value for the charging current is also kept the same as of simulation 30A, however, the reference for ESS is generated by top-layer droop control. The HIL setup is illustrated in Fig. 10. The HIL results show that the controller performed up to the mark in real time as well. The zoomed-in parts of the different sub-plots depict the transient behavior of the state variables. It can be verified that DC bus voltage can regulate to its desired value. Moreover, the effective charging and discharging of the battery and SC proves the power-sharing concept depending on the storage system's dynamic response. The SC can provide a fast response to cope with sudden load changes. The stable charging current for the EV verifies the idea of integrating EVs with microgrids and also provides the supporting argument for the successful development of an EV charging controller.

VI. CONCLUSION AND FUTURE WORK

The research introduces a two-layer control structure for optimal power sharing and a nonlinear switch controller for diverse power converters within a DC microgrid designed for e-mobility. This microgrid configuration integrates ESS and advanced converter topologies like FSIBB and DAB, offering a broad operating range, bidirectional power flow, and seamless interaction with EVs. The paper extensively discusses the mathematical analysis of the control design and closed-loop stability. Leveraging Lyapunov's theory, the global stability of the system is explored, affirming its stability under the proposed control measures. MATLAB/Simulink-based simulations are executed under various conditions to validate the controller performance. The results affirm that the primary control strategy adeptly shares load power by efficiently managing ESS charge and discharge cycles. Notably, the

SC exhibits swift dynamic responses, compensating for the battery's slower dynamics, thereby confirming the efficacy of the enhanced droop control strategy. The adaptive nonlinear controller, evidenced by effective trajectory tracking with fast settling times and low steady-state, further substantiates the proposed approach's merit. Robustness testing confirms the self-compensation capability of the nonlinear controller, showcasing its resilience in managing unknown disturbances while minimizing controller gains. The proposed methodology prevents the overestimation of the gains and provides robustness against unforeseen disturbances without observer design. The comparative analysis with state-of-the-art control methods concludes that the proposed controller has optimized response and also overcomes the issues related to traditional methods. Furthermore, HIL tests, executed using the Typhoon HIL 404 device, validate the real-time performance of the proposed controller. The real-time results provide the validity of the proposed method for practical implementations. This work will be expanded in future endeavors by incorporating advanced control algorithms and setting up a small-scale prototype. Additionally, exploring the integration of DC microgrids and EVs with conventional power grids, coupled with robust control systems, presents an intriguing avenue for future research.

REFERENCES

[1] F. S. Al-Ismail, "DC microgrid planning, operation, and control: A comprehensive review," *IEEE Access*, vol. 9, pp. 36154–36172, 2021.

[2] T. Dragicevic, X. Lu, J. C. Vasquez, and J. M. Guerrero, "DC microgrids—Part I: A review of control strategies and stabilization techniques," *IEEE Trans. Power Electron.*, vol. 31, no. 7, pp. 4876–4891, Jul. 2016.

[3] T. Dragicevic, X. Lu, J. C. Vasquez, and J. M. Guerrero, "DC microgrids—Part II: A review of power architectures, applications, and standardization issues," *IEEE Trans. Power Electron.*, vol. 31, no. 5, pp. 3528–3549, May 2016.

[4] H. Masrur, M. Shafie-Khah, M. J. Hossain, and T. Senjyu, "Multi-energy microgrids incorporating EV integration: Optimal design and resilient operation," *IEEE Trans. Smart Grid*, vol. 13, no. 5, pp. 3508–3518, Sep. 2022.

[5] R. H. Ashique, Z. Salam, M. J. Bin Abdul Aziz, and A. R. Bhatti, "Integrated photovoltaic-grid DC fast charging system for electric vehicle: A review of the architecture and control," *Renew. Sustain. Energy Rev.*, vol. 69, pp. 1243–1257, Mar. 2017.

[6] L. E. Zubieta, "Are microgrids the future of energy?: DC microgrids from concept to demonstration to deployment," *IEEE Electrific. Mag.*, vol. 4, no. 2, pp. 37–44, Jun. 2016.

[7] F. Gao, R. Kang, J. Cao, and T. Yang, "Primary and secondary control in DC microgrids: A review," *J. Modern Power Syst. Clean Energy*, vol. 7, no. 2, pp. 227–242, Mar. 2019.

[8] J. Liu, W. Zhang, and G. Rizzoni, "Robust stability analysis of DC microgrids with constant power loads," *IEEE Trans. Power Syst.*, vol. 33, no. 1, pp. 851–860, Jan. 2018.

[9] S. Singh, A. R. Gautam, and D. Fulwani, "Constant power loads and their effects in DC distributed power systems: A review," *Renew. Sustain. Energy Rev.*, vol. 72, pp. 407–421, May 2017.

[10] L. Benadero, R. Cristiano, D. J. Pagano, and E. Ponce, "Nonlinear analysis of interconnected power converters: A case study," *IEEE J. Emerg. Sel. Topics Circuits Syst.*, vol. 5, no. 3, pp. 326–335, Sep. 2015.

[11] T. Dragicevic, J. M. Guerrero, J. C. Vasquez, and D. Škrlec, "Supervisory control of an adaptive-droop regulated DC microgrid with battery management capability," *IEEE Trans. Power Electron.*, vol. 29, no. 2, pp. 695–706, Feb. 2014.

[12] M. Saleh, Y. Esa, and A. Mohamed, "Centralized control for DC microgrid using finite state machine," in *Proc. IEEE Power Energy Soc. Innov. Smart Grid Technol. Conf. (ISGT)*, Apr. 2017, pp. 1–5.

[13] A. Tah and D. Das, "An enhanced droop control method for accurate load sharing and voltage improvement of isolated and interconnected DC microgrids," *IEEE Trans. Sustain. Energy*, vol. 7, no. 3, pp. 1194–1204, Jul. 2016.

[14] X. Li, L. Guo, S. Zhang, C. Wang, Y. W. Li, A. Chen, and Y. Feng, "Observer-based DC voltage droop and current feed-forward control of a DC microgrid," *IEEE Trans. Smart Grid*, vol. 9, no. 5, pp. 5207–5216, Sep. 2018.

[15] M. Mokhtar, M. I. Marei, and A. A. El-Sattar, "An adaptive droop control scheme for DC microgrids integrating sliding mode voltage and current controlled boost converters," *IEEE Trans. Smart Grid*, vol. 10, no. 2, pp. 1685–1693, Mar. 2019.

[16] L. Herrera, W. Zhang, and J. Wang, "Stability analysis and controller design of DC microgrids with constant power loads," *IEEE Trans. Smart Grid*, vol. 8, no. 2, pp. 881–888, Mar. 2017.

[17] Z. Karami, Q. Shafiee, S. Sahoo, M. Yaribeygi, H. Bevrani, and T. Dragicevic, "Hybrid model predictive control of DC–DC boost converters with constant power load," *IEEE Trans. Energy Convers.*, vol. 36, no. 2, pp. 1347–1356, Jun. 2021.

[18] R. R. Deshmukh, M. S. Ballal, and H. M. Suryawanshi, "A fuzzy logic based supervisory control for power management in multibus DC microgrid," *IEEE Trans. Ind. Appl.*, vol. 56, no. 6, pp. 6174–6185, Nov. 2020.

[19] N. Chettibi, A. Mellit, G. Sulligoi, and A. Massi Pavan, "Adaptive neural network-based control of a hybrid AC/DC microgrid," *IEEE Trans. Smart Grid*, vol. 9, no. 3, pp. 1667–1679, May 2018.

[20] V. Chapparya, A. Dey, and S. P. Singh, "A novel non-isolated boost-zeta interleaved DC–DC converter for low voltage bipolar DC micro-grid application," *IEEE Trans. Ind. Appl.*, pp. 1–11, 2023.

[21] Z. Xiao, W. Lei, G. Gao, X. Zhang, and L. Hu, "Dual-terminal voltage feedforward based direct power control scheme and stability analysis of dual active bridge converter in DC microgrid systems," *IEEE Trans. Power Electron.*, vol. 38, no. 4, pp. 4475–4492, Apr. 2023.

[22] D. Das, M. J. Hossain, S. Mishra, and B. Singh, "Bidirectional power sharing of modular DABs to improve voltage stability in DC microgrids," *IEEE Trans. Ind. Appl.*, vol. 58, no. 2, pp. 2369–2377, Mar. 2022.

[23] H.-S. Lee and J.-J. Yun, "High-efficiency bidirectional buck–boost converter for photovoltaic and energy storage systems in a smart grid," *IEEE Trans. Power Electron.*, vol. 34, no. 5, pp. 4316–4328, May 2019.

[24] S. R. Khasim, C. Dhanamjayulu, and S. M. Muyeen, "A single inductor multi-port power converter for electric vehicle applications," *IEEE Access*, vol. 11, pp. 3367–3385, 2023.

[25] Q. Xu, N. Vafamand, L. Chen, T. Dragicevic, L. Xie, and F. Blaabjerg, "Review on advanced control technologies for bidirectional DC/DC converters in DC microgrids," *IEEE J. Emerg. Sel. Topics Power Electron.*, vol. 9, no. 2, pp. 1205–1221, Apr. 2021.

[26] M. M. Mardani, M. H. Khooban, A. Masoudian, and T. Dragicevic, "Model predictive control of DC–DC converters to mitigate the effects of pulsed power loads in naval DC microgrids," *IEEE Trans. Ind. Electron.*, vol. 66, no. 7, pp. 5676–5685, Jul. 2019.

[27] Y. Yu, G.-P. Liu, and W. Hu, "Coordinated distributed predictive control for voltage regulation of DC microgrids with communication delays and data loss," *IEEE Trans. Smart Grid*, vol. 14, no. 3, pp. 1708–1722, May 2023.

[28] V. Kumar, S. R. Mohanty, and S. Kumar, "Event trigger super twisting sliding mode control for DC micro grid with matched/unmatched disturbance observer," *IEEE Trans. Smart Grid*, vol. 11, no. 5, pp. 3837–3849, Sep. 2020.

[29] M. S. Sadabadi, Q. Shafiee, and A. Karimi, "Plug-and-play robust voltage control of DC microgrids," *IEEE Trans. Smart Grid*, vol. 9, no. 6, pp. 6886–6896, Nov. 2018.

[30] S. S. Zehra, A. Ur Rahman, and I. Ahmad, "Fuzzy-barrier sliding mode control of electric-hydrogen hybrid energy storage system in DC microgrid: Modelling, management and experimental investigation," *Energy*, vol. 239, Jan. 2022, Art. no. 122260.

[31] Q. Xu, X. Hu, P. Wang, J. Xiao, P. Tu, C. Wen, and M. Y. Lee, "A decentralized dynamic power sharing strategy for hybrid energy storage system in autonomous DC microgrid," *IEEE Trans. Ind. Electron.*, vol. 64, no. 7, pp. 5930–5941, Jul. 2017.

[32] S. Laghrouche, M. Harmouche, Y. Chitour, H. Obeid, and L. M. Fridman, "Barrier function-based adaptive higher order sliding mode controllers," *Automatica*, vol. 123, Jan. 2021, Art. no. 109355.

[33] B. Wang, U. Manandhar, X. Zhang, H. B. Gooi, and A. Ukil, "Deadbeat control for hybrid energy storage systems in DC microgrids," *IEEE Trans. Sustain. Energy*, vol. 10, no. 4, pp. 1867–1877, Oct. 2019.

[34] M. J. Carrizosa, A. Iovine, G. Damm, and P. Alou, "Droop-inspired nonlinear control of a DC microgrid for integration of electrical mobility providing ancillary services to the AC main grid," *IEEE Trans. Smart Grid*, vol. 13, no. 5, pp. 4113–4122, Sep. 2022.

[35] M. H. Rashid, *Power Electronics Handbook*. Oxford, U.K.: Butterworth-Heinemann, 2017.

[36] V. Castiglia, N. Campagna, A. O. D. Tommaso, R. Miceli, C. Nevoloso, F. Pellitteri, C. Puccio, and F. Viola, "Modeling, simulation, and characterization of a supercapacitor in automotive applications," *IEEE Trans. Ind. Appl.*, vol. 58, no. 2, pp. 2421–2429, Mar. 2022.

[37] A. U. Rahman, N. Campagna, A. Di Tommaso, R. Miceli, A. Damiano, and A. Floris, "Advanced control analysis of single inductor four switch non-inverting buck-boost converter for energy storage units," in *Proc. Int. Conf. Clean Elect. Power (ICCEP)*, Jun. 2023, pp. 267–272.

[38] J. Mahdavi, A. Emaadi, M. Bellar, and M. Ehsani, "Analysis of power electronic converters using the generalized state-space averaging approach," *IEEE Trans. Circuits Syst. I, Fundam. Theory Appl.*, vol. 44, no. 8, pp. 767–770, Aug. 1997.

[39] S. Shao, L. Chen, Z. Shan, F. Gao, H. Chen, D. Sha, and T. Dragicevic, "Modeling and advanced control of dual-active-bridge DC–DC converters: A review," *IEEE Trans. Power Electron.*, vol. 37, no. 2, pp. 1524–1547, Feb. 2022.

[40] M. Arsalan, R. Iftikhar, I. Ahmad, A. Hasan, K. Sabahat, and A. Javeria, "MPPT for photovoltaic system using nonlinear backstepping controller with integral action," *Sol. Energy*, vol. 170, pp. 192–200, Aug. 2018.

AQEEL UR RAHMAN (Student Member, IEEE) received the B.S. degree from Mirpur University of Science and Technology, in 2017, the M.S. degree in electrical engineering with a specialization in power and control systems from the School of Electrical Engineering and Computer Science, National University of Sciences and Technology (NUST), Islamabad, Pakistan, in 2019. He is currently pursuing the dual Industrial Ph.D. degree with the University of Palermo and Prysmian Electronics. His research interests include control of renewable energies, modern control of power converters, DC microgrids, nonlinear control of electric vehicles, and control applications in energy storage units.

NICOLA CAMPAGNA (Member, IEEE) received the M.S. and Ph.D. degrees in electrical engineering from the University of Palermo, Italy, in 2019 and 2023, respectively. In 2019, he joined the Sustainable Development and Energy Saving Laboratory, University of Palermo, focusing his research activities on the design of power electronics converter and energy storage systems. In 2022, he joined the Electrotechnical Engineering Department, Nova University Lisbon, involved in the design of wireless power transfer systems for automotive. He is currently a Researcher with the Department of Engineering, University of Palermo.

ANTONINO OSCAR DI TOMMASO was born in Tübingen, Germany, in June 1972. He received the master's and Ph.D. degrees in electrical engineering from the University of Palermo, Italy, in 1999 and 2004, respectively. He was a Post Ph.D. Fellow of electrical machines and drives with the Department of Electrical Engineering, University of Palermo, from 2004 to 2006. He is currently an Associate Professor of electrical machines with the Department of Engineering, University of Palermo. His research interests include electrical machines, drives, diagnostics on power converters, and diagnostics and design of electrical rotating machines.

FILIPPO PELLITTERI (Member, IEEE) received the B.S. and M.S. degrees in electronics engineering and the Ph.D. degree in electrical engineering from the University of Palermo, Italy, in 2009, 2012, and 2016, respectively. He undertook internships at STMicroelectronics, Catania, Italy, and The University of Auckland, New Zealand, in 2012 and 2014, respectively. From 2016 to 2019, he was a Postdoctoral Research Fellow with the School of Aerospace Engineering, Sapienza University of Rome, Italy, in the framework of a contract sponsored by European Space Agency. He is currently an Assistant Professor with the Department of Engineering, University of Palermo. His research interests include analysis, modeling and design of power converters, and characterization of electronic devices, with application to renewable energy systems, electric vehicles, and microgrids.

ROSARIO MICELI (Member, IEEE) received the B.S. degree in electrical engineering and the Ph.D. degree from the University of Palermo, Palermo, Italy, in 1982 and 1987, respectively. He is currently a Full Professor of electrical machines with the Polytechnic School, University of Palermo. He is the Personnel in Charge of the Sustainable Development and Energy Savings Laboratory of the Palermo Athenaeum. His research interests include mathematical models of electrical machines, drive system control, and diagnostics, renewable energies, and energy management. He is a reviewer of IEEE TRANSACTIONS ON INDUSTRIAL ELECTRONICS and IEEE TRANSACTIONS ON INDUSTRY APPLICATIONS.

● ● ●